Unveiling the mechanism of the triethyl phosphate hydrolysis reaction in the synthesis of the sol-gel-derived 58S bioactive glass

O.M. Vargas Machuca Bueno [a], [*], [d], M.A. San-Miguel [b], C.A. Bertran [b], E. Zacarias da Silva [a], J.H. Lopes [c], [d]

[a] Institute of Physics "Gleb Wataghin", UNICAMP, 13083-859, Campinas, SP, Brazil
[b] Department of Physical Chemistry, Institute of Chemistry, University of Campinas — UNICAMP, P.O. Box 6154, 13083-970, Campinas, SP, Brazil
[c] Department of Chemistry, Division of Fundamental Sciences (IEF), Aeronautics Institute of Technology — ITA, 12228-900, Sao Jose Dos Campos-SP, Brazil

ARTICLE INFO

ABSTRACT

The sol-gel method is one of the most used methods due to its outstanding capacity to obtain alkaline-earth phosphosilicate bioactive glass with high bioactivity. This efficient synthesis method involves several stages constituted by intermediate chemical reactions, which are governed by mechanisms and kinetic parameters that lead to the formation of the precursor gel of the vitreous matrix. Although the sol-gel method has been widely used for the preparation of materials, some steps are still not completely understood and that affect the final properties of the synthesized materials. For instance, the hydrolysis reaction of triethyl phosphate (TEP) which, similarly to tetraethyl orthosilicate (TEOS), is assumed to be complete in the stage of formation of the precursor gel of the glass matrix. Furthermore, the SN_2-type mechanism for the hydrolysis of TEP is widely assumed. However, the absence of studies that support these presumptions fully justifies the use of theoretical methods to gain information about the hydrolysis of TEP within the sol-gel synthesis of 58S bioactive glass. Density functional theory (DFT) and molecular dynamics (MD) simulations were used to study the reaction mechanisms and kinetic behavior of TEP hydrolysis. Our results show that the TEP hydrolysis reaction is very slow in its three stages, occurring not only via the SN_2 mechanism with configuration inversion (SN_2-I), as is commonly reported in the literature, but also via SN_2 with configuration retention (SN_2-R). Furthermore, it was found that the hydrolysis reaction via SN_2-I occurs with faster kinetics than SN_2-R. This behavior was observed for the three stages of TEP hydrolysis, both in protonated and non-protonated solutions. Based on our findings on the mechanisms and kinetics of triethyl phosphate hydrolysis reactions, a simple chemical model for the formation of calcium pyrophosphate crystalline domains in 58S sol-gel bioactive glass was proposed. In our model, TEOS undergoes rapid hydrolysis, followed by immediate condensation leading to the formation of three-dimensional silica gels, that permeate non-hydrolyzed TEP molecules due to their slow kinetic rate. This mismatch between the reactions of precursor alkoxides in acidic medium, results in a strong tendency in the formation of a glassy microstructure with low structural homogeneity characterized by crystalline domains of calcium pyrophosphate permeated by a silica-rich glass matrix.

© 2022 Elsevier Ltd. All rights reserved.

1. Introduction

The sol-gel method is one of the well-established synthetic approaches to prepare the different types of bioceramics for the repair, reconstruction, and replacement of diseased or damaged parts of the body [1—5]. Bioactive glasses are by far the most promising bioceramics for bone healing, due to their bioactivity and the proven ability of ionic dissolution products released to stimulate cell genes towards a path of regeneration and self-repair [2—4,6,7]. Among the numerous glass compositions for biomedical applications described in the literature, sol-gel-derived 58S bioactive glass has been extensively studied due to its high bioactivity and excellent processing properties [8—11]. Furthermore, it has allowed the development of bioactive scaffolds based on glasses and their polymeric composites with structures exhibiting tailored porosity, pore size, and interconnectivity [7,12—15].

---

* Corresponding author.
E-mail address: ottovmb@ifi.unicamp.br (O.M. Vargas Machuca Bueno).
[d] These authors contributed equally.

A brief review of the literature reveals that the phosphorus precursor used in the sol-gel method for preparing bioactive glasses plays a fundamental role in the structure and texture of the synthesized material [16,17]. Among the phosphorus precursors available, triethyl phosphate (TEP) is undoubtedly the most common source used in the sol-gel route for the synthesis of sol-gel bioactive glasses and other materials used for different purposes [10,18,19]. Notwithstanding, the behavior of this P-alkoxide during the sol-gel steps has not yet been fully understood [18–20]. For instance, several studies have assumed that the TEP hydrolysis reaction occurs partially or completely in an acid medium during the evolution of the sol toward gel, which leads to a distribution of phosphate species throughout the glassy matrix, modifying the silica backbone and/or isolated species associated with calcium ions [16,17,19]. However, some experimental evidence suggests an opposite behavior for TEP behavior [19]. Apparently, the TEP hydrolysis kinetics is slow, which would be directly associated with phase segregation and the formation of phosphorus-rich crystalline domains into the matrix of alkaline-earth phosphosilicate bioactive glass [18,19]. In addition, previous studies show a strong dependence between the appearance of calcium pyrophosphate domains within the matrix and the behaviour exhibited by triethyl phosphate molecules during the evolution of the sol towards the glass precursor gel, i.e., in the hydrolysis and condensation reactions [18,19]. The presence of these microstructural heterogeneities modifies the solubility of bioactive glass, affecting the ability to release biologically active species and hence negatively influencing bioactivity [21].

The present work presents and discusses the results of a comprehensive study on the reaction mechanism and the kinetic parameters of the hydrolysis reaction of TEP in similar conditions those found during the early stages of the sol-gel method for 58S bioactive glass synthesis. An efficient and accurate way to investigate the hydrolysis reaction of triethyl phosphate is through theoretical methods such as the DFT method [20,22–24]. Nonetheless, there are very few theoretical studies by DFT dedicated to the investigation of the hydrolysis reaction of TEP in aqueous solution, most of which are aimed at the study of pyrolysis reactions [20,22], complexes with alkaline metals in gas phase [23] or conformation studies [24]. Bearing this in mind, we explore the hydrolysis reaction of TEP in an aqueous solution under neutral and acidic conditions using the DFT method. Initially, we will address the structural behavior of TEP by classical molecular dynamics, while the DFT method will be used to study chemical reactions to find the minimum energy path within the IRC approach and the reaction rates for each stage of TEP hydrolysis. Ultimately, we will use the reaction mechanism data and kinetic parameters to speculate the formation of crystalline clusters embedded in the vitreous microstructure, which negatively impacts the release of biologically important species for tissue repair and wound healing and, consequently, bioactivity.

2. Methodology

2.1. Density functional theory

The quantum calculations were performed with the Gaussian 09 quantum chemistry package, version D.01 [25]. In all chemical reactions involved in the study, a relaxed scan potential energy surface was made in the gas phase to find structures close to the transition state (TS). In all systems, the optimized geometries, harmonic vibrational frequencies, and zero-point energy (ZPE) of all the stationary points for reactants, transition states (TSs), and products were calculated at the wB97XD/6−311++G (d,f) level of theory. The intrinsic reaction coordinate (IRC) [26–28] method was used to verify that the TS structures correspond to the structures of the reactive and products designated. In all cases, IRC calculations were obtained with irc (calcfc, recalc = 10, maxpoints = (400 or 600), maxcycle = 40, tight, cartesian, stepsize = (7 or 5), lqa). The structures of one end of the IRC paths (reactants) were optimized to calculate the rates of reaction. Conventional transition state (TS) theory [28] was used to calculate the reaction rate at 298.15 K, considering the standard state 1 M for all cases (c = 1, Equation (1)). Second-order rate constants were calculated for these reactions according to Equations (1) and (2). In all cases, the quantum mechanical tunneling effect was carried out using the Wigner method [29,30].

$$K(T) = l \left[1 + \left(\frac{1}{24} \right) \left[1.44 \frac{v_i}{T} \right]^2 \right] \frac{K_B T}{hc^o} exp \left[\frac{-\Delta G^{\ddagger}}{RT} \right] \tag{1}$$

$$\Delta G^{\ddagger} = \sum_{TS} (E_0 + G_{corrected})_{TS} - \sum_{reactants} (E_0 + G_{corrected})_{reactants} \tag{2}$$

Where l represents the reaction path degeneracy, accounting for the number of equivalent reaction paths, and it is set to $l = 1$ for all calculations. K_b and h are the Boltzmann and Planck constants, respectively. V_i is the imaginary vibrational wave number in units of cm^{-1} related to the additional chemical bond of the structure of the transition state. $\Delta G^{\ddagger}$ is the activation energy barrier, E_o is the total electronic energy at $T = 0K$, and $G_{corrected}$ is the thermal correction of the Gibbs free energy.

2.2. Classical molecular dynamics simulations

Molecular dynamics (MD) simulations were carried out using the classic DLPOLY package [31], in the canonical ensemble (NVT) with the Nosé-Hoover thermostat [32]. Initial velocities were established using the Boltzmann distribution. The equations of motion were integrated using the velocity-verlet algorithm with a time step of 1 fs. The simulations were extended up to 60 ns. All initial settings were generated with the Packmol package [33]. The LigParGen program [34] was used to generate the OPLS-aa force field [35] for TEP, considering the partial charge correction 1.4*CMP1A-LBCC [36]. Protonated and non-protonated solutions were simulated with explicit water molecules using the Transferable Intermolecular Potential-Three Point (TIP3P) model with flexible OH bonds [37,38]. In the case of the protonated solution, the protons were simulated assuming the formation of hydronium ions, and the parameters were taken from Urata et al. [39] and Shengting et al. [40] The parameters for nitrate ion NO_3^- were taken from Somisetti et al. [41] and Cadena et al. [42] The simulation box was defined from the experimental density of the precursor solution of the sol-gel method (1.002 g cm^{-3}) [18].

For the free energy studies, metadynamics MD simulations were performed with LAMMPS code [43] patched with PLUMED 2.5.4 plugin [44] in the ensemble NPT. Well-tempered metadynamics simulations were used in all cases [45,46]. The dihedral angles C−C−O−P were used as collective variables (CV) to achieve changes of conformers in the TEP molecule. Meta-MD parameters were defined with the Gaussian deposition every 400 timesteps, starting hill height of 0.3 kcal mol^{-1}, gaussian widths of 0.4 radians, bias factor of 5.0, and ΔT = 300 K. The error associated with free energy was obtained by post-processing of well-tempered metadynamics simulation, using the block-analysis method as a function of the collective variable [47].

O.M. Vargas Machuca Bueno, M.A. San-Miguel, C.A. Bertran et al.

*Materials Today Chemistry 24 (2022) 100929*

3. Results and discussion

3.1. Structural behavior of the TEP molecules in solution

The dynamical behavior of TEP molecules in an aqueous solution has been studied from MD simulations (Fig. 1a). The quantitative study of the grouping of TEP molecules was performed using the DFSCLUSTERING algorithm [47] implemented in PLUMED. The results show that, throughout the simulation, the TEP molecules remain predominantly isolated from each other, also showing a minimal amount of grouping of two TEP molecules (see Figure SM1). Therefore, this result would allow us to study the hydrolysis reactions of TEP with DFT methods without losing any interaction effect that could arise if the TEP grouping were dominant (Fig. 1b). This would even allow the use of implicit solvent models with and without some explicit water molecules, without losing validity.
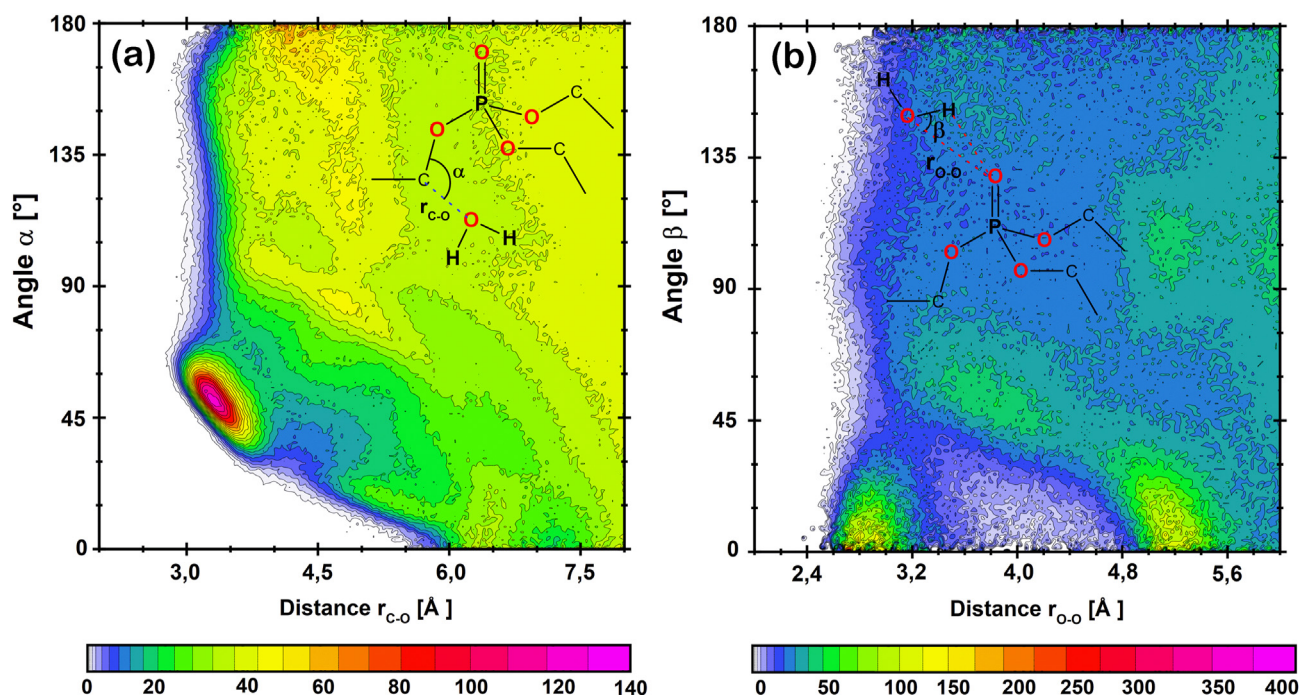
On the other hand, the structural analysis of the TEP molecules was analyzed using Combined Distribution Functions (CDF) available in TRAVIS code [48]. Two important factors were considered: (i) preferential orientation of the solvent (water) concerning the $-CH_2-$ group (Fig. 2a), and (ii) hydrogen bond (H-bond) between solute-solvent (Fig. 2b).

The results reveal that the water molecules can reach a maximum approximation of 3 Å of the carbon of the $-CH_2-$ groups approaching with an angle α around 60°. Furthermore, as water molecules approach the $-CH_2-$ group and reach distances between 3 and 4 Å, it is possible to observe that the H_2O molecules are preferentially oriented in the angular range between 40° and 60° and, to a lesser extent, oriented in the angular range between 85°
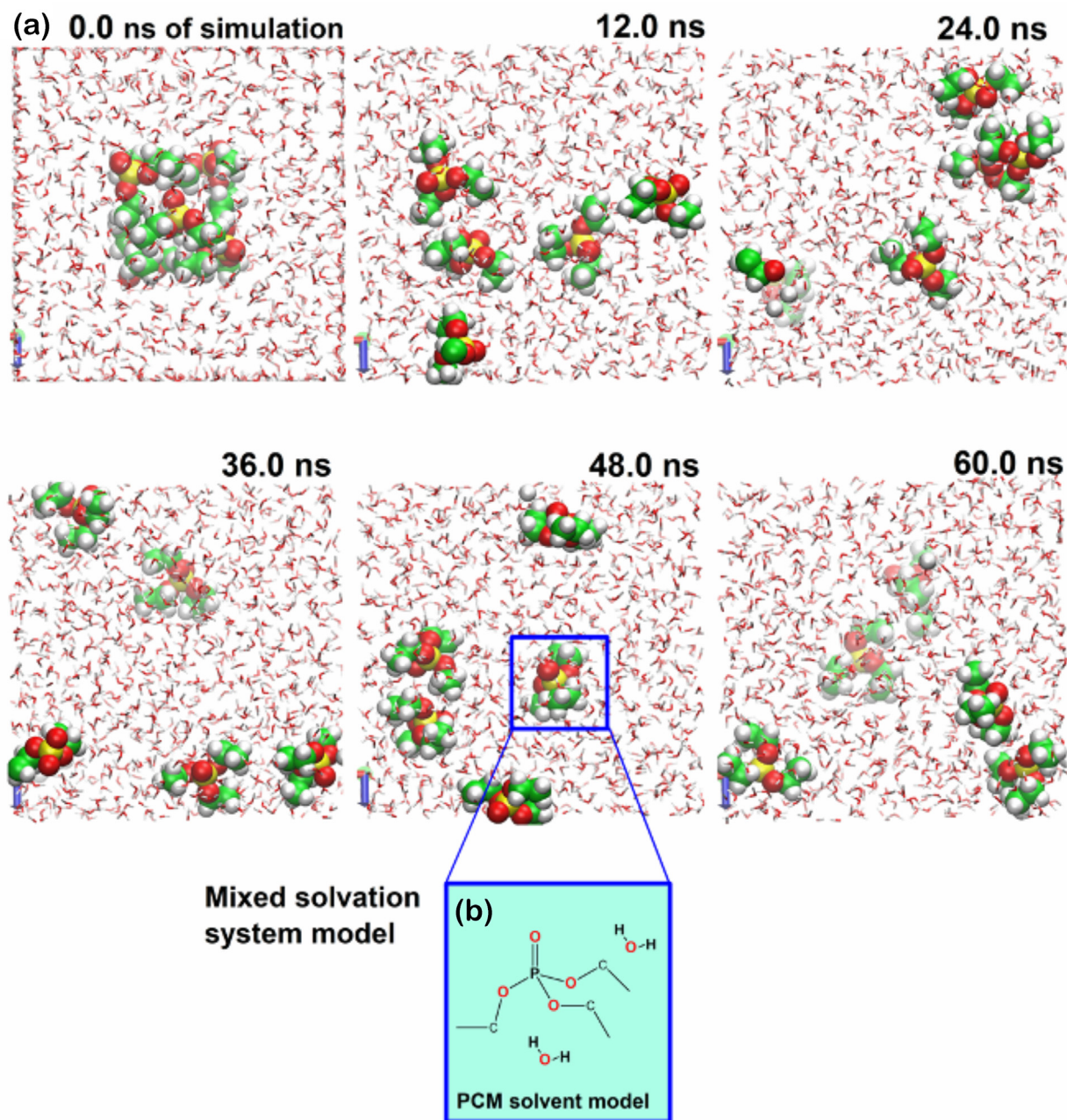
Fig. 1. (a) Visual inspection of the simulation of the precursor solution of 58S bioactive glass. The simulations were spanned up to 60 ns. (b) System model: mixed solvation, within the DFT methodology.

O.M. Vargas Machuca Bueno, M.A. San-Miguel, C.A. Bertran et al.

*Materials Today Chemistry 24 (2022) 100929*

Fig. 2. Combined Distribution Function (CDF) with RDF and ADF channels to study nucleophilic attacks and H-bond interactions. (a) Study of the interaction between $-CH_2-$ carbon and water molecules, with one channel being a distance (r_{c-o}) and the other one being an angle (α). (b) Study of H-bond interaction between the $-P=O$ group and water molecules, with one channel being a distance (r_{o-o}) and the other one being an angle (β).

and 165°. These results suggest that water molecules can attack $-CH_2-$ groups basically by two different pathways. Analyzing these pathways, it is observed that TEP adopts more than one structural conformation to facilitate it. The first pathway occurs when $-CH_2-$ and $-P=O$ groups are close to each other. In this case, a water molecule can interact with the $-P=O$ group. The second pathway occurs when the $-CH_2-$ group is far from the $-P=O$ group. Thus, considering these results, in the DFT studies, different potential energy surface (PES) scans will be performed around these routes to find the transition state (TS) structures.

The ability to form hydrogen bonds (H-bonds) between the solvent and solute under acidic conditions has also been investigated by monitoring the approaching distance and relative orientation using the r_{o-o} and β variables (Fig. 2b). The analysis reveals the formation of a zone that corresponds to the formation of H-bonds ($r_{o-o} < \sim 3.0$ Å and $\beta < \sim 20°$). This suggests the formation of protonated TEP (TEP$-H^+$). This result agrees with the experimental study carried out by Lyznicki et al. [41], where the formation of TEP-H^+ is also suggested. Based on these results, for DFT studies, our protonated system will be defined by leaving a proton (H^+) near the O=P$-$ group. Then, the proton of the water in the first solvation layer is restricted to a certain orientation range concerning the axis of the O=P$-$ group to interact with the oxygen O=P$-$. Two variables were defined (r_{H-O} and θ) to show these orientations, one that informs the proximity between them, and the other one is the orientation of the proton (H^+) concerning the group O=P$-$ (see Figure SM2). The results show that the proton must be oriented between 0 and 45° to interact with the oxygen O=P$-$. Thus, for the studies of systems protonated by DFT, protons (H^+) will be defined within these orientations, placing water molecules explicitly if necessary to ensure this orientation.

Complimentary, the energy barriers in the conformational changes of the TEP molecule were analyzed using Meta-MD simulations. The results show that the TEP molecule has a great facility to adapt different conformers throughout the simulation (Fig. 3).
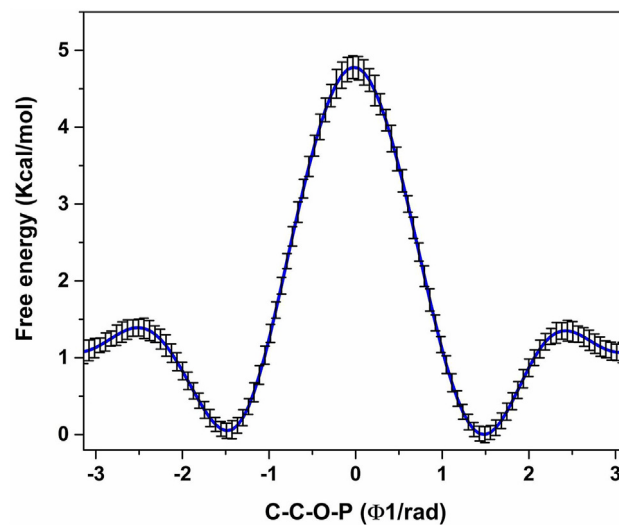
Fig. 3. Free energy profile obtained from simulations of classical molecular dynamics with well-tempered metadynamics technique. The collective variable was defined using the dihedral angle C$-$C$-$O$-$P.

The energy barriers to go from one conformer to another vary around 1$-$5 kcal mol^{-1}. Hence, it is necessary to consider more than one conformer of triethyl phosphate in the kinetic study by DFT. The behavior of conformers in the second and third hydrolysis is very similar to that of the first hydrolysis (see Figure SM3). Using Meta-MD simulations with 2 CVs (P$-$O$-$C$-$C) revealed the presence of at least eight different conformers with similar relative stability and separated by activation energy barriers between ~1 and ~8 kcal mol^{-1} (see Figure SM4). The low activation energy barrier shows that the hydrolysis reaction could occur with any of these conformers. Therefore, the nucleophile that enters near or far

O.M. Vargas Machuca Bueno, M.A. San-Miguel, C.A. Bertran et al.

Materials Today Chemistry 24 (2022) 100929

from the O=P− group to attack the −CH$_2$− carbon would have a similar chance to promote a hydrolysis reaction.

3.2. Kinetic analysis of the TEP hydrolysis reaction

3.2.1. Reaction mechanisms in the gas phase

To gain insights into the reaction mechanism of TEP hydrolysis reactions, we first explore the interaction between a TEP and a water molecule using DFT calculations. The studies began with the search for the structures of the transition state (TS) in the gas phase. The exploration of the potential energy surface (PES) around the two routes suggested by the MD simulations were explored (see Figure SM5-SM8). Several TS structures were found exploring the different TEP conformers. Using the IRC method, two different behaviors in their reaction mechanism were observed. The TS structures lead to nucleophilic substitution SN$_2$−I and SN$_2$−R
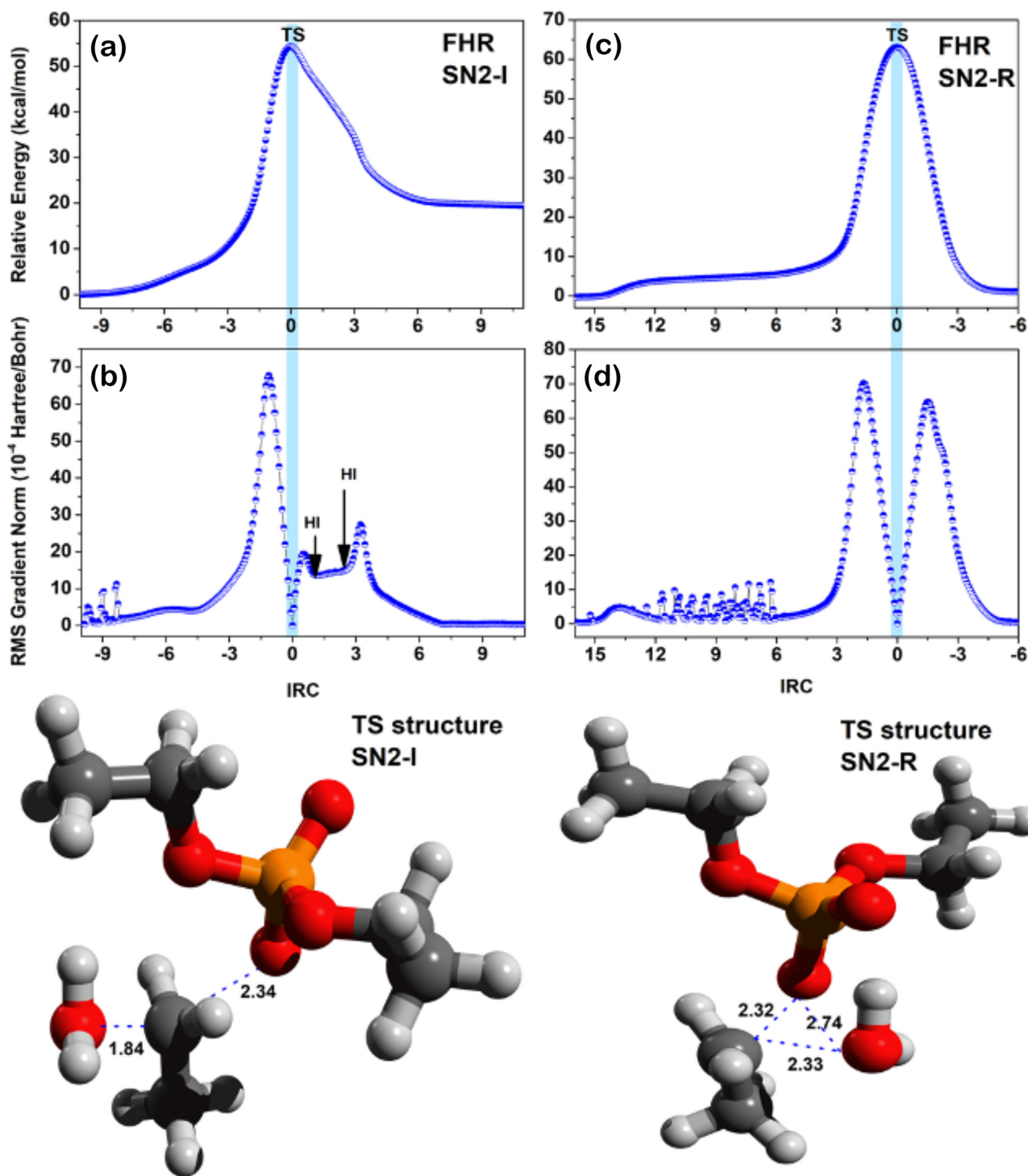
Fig. 4. Path energy profile and root mean squared (RMS) gradient norm along with IRC. The reaction pathway for the reaction of hydrolysis of the TEP (FHR) in the gas phase is shown. All calculations were computed at the wB97XD/6−311++G** theory level. (a) and (b) represent the IRC and RMS for the SN2−I mechanism, respectively. (c) and (d) represent the IRC and RMS for the SN2-R mechanism, respectively. The molecules represent the TS structures for both cases (SN$_2$−I and SN$_2$−R).

O.M. Vargas Machuca Bueno, M.A. San-Miguel, C.A. Bertran et al.

Materials Today Chemistry 24 (2022) 100929

mechanisms, where SN_2-I is a mechanism with configuration inversion and SN_2-R is with configuration retention. As an example, IRC results for the first hydrolysis reaction (FHR) are presented (Fig. 4). Similar behavior can be observed for the second hydrolysis reaction (SHR), third hydrolysis reaction (THR) in all TEP conformers (see Figure SM9).

The root mean squared (RMS) gradient norm along IRC confirms that the reactions with the SN_2-I mechanism indicate the formation of hidden intermediaries (HIs) at all stages (FHR, SHR and THR). The HIs are related to the presence of a proton (H^+) between oxygen atoms in (i) the formation of protonated alcohol ($CH_3-CH_2-OH_2^+$), and (ii) when the proton is trapped between the alcohol and the TEP ($O=PO-H-OH-CH_2-CH_3$) (see Figure SM10). For example, FHR shows a minimum local in RMS of ~1.1 related to an HI, which corresponds to the formation of a protonated alcohol, and RMS of ~2.7 related to the proton trapped between the protonated alcohol and the TEP (Fig. 4a and b). While for THR, the local minimum of RMS ~1.1 is also due to the presence of a proton trapped between the alcohol and the TEP, and the local minimum in RMS ~2.3 indicates the formation of protonated alcohol (see Figure SM9b).

On the other hand, in the SN_2-R mechanisms, it is possible to notice the absence of HI, thus in all the hydrolysis stages. For instance, there are no local minima that indicate the formation of HI for FHR (Fig. 4c and d). Furthermore, it is also observed that the formation of alcohol occurs without the formation of the protonated alcohol as an intermediate.

In general, when comparing all the IRC data for the different TEP conformers and in its three stages of hydrolysis (see Figure SM9), it is possible to find characteristics that allow drawing some conclusions. Hydrolysis reactions with the SN_2-I mechanism tend to exhibit HIs related to the formation of protonated alcohol. Conversely, the presence of HIs is negligible and alcohol formation occurs directly if the reaction occurs with SN_2-R. It is also observed that in some cases of SN_2-I mechanism, the IRC shows that the hydrolysis of TEP occurs endothermically due to the formation of protonated alcohol as a final product (Fig. 4a and Figure SM9b and SM9e). The proton in $CH_3-CH_2-OH_2^+$ is not propagated by the medium due to the lack of solvent. This behavior makes it clear that it is necessary to consider explicit solvent molecules to improve the study of the reaction mechanism.

3.2.2. Reaction mechanisms in solution (PCM solvent model)

In addition to using the PCM model, we also considered a second strategy including explicitly more water molecules to analyze the solvent effects on hydrolysis reaction. Two approaches were
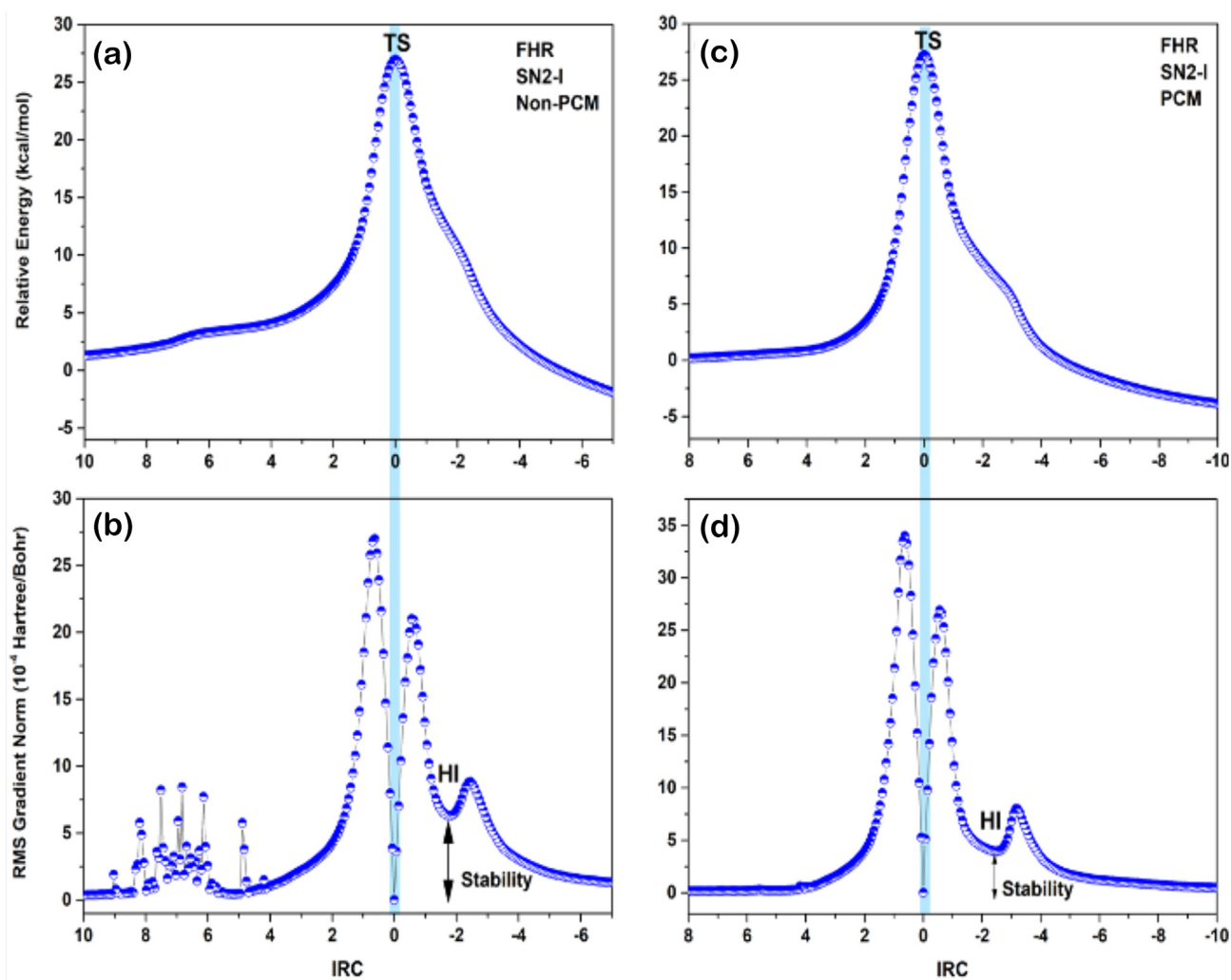

Fig. 5. IRC path energy profile and RMS gradient norm along with IRC. It is shown the reaction pathway for the reaction of hydrolysis of the TEP (FHR) with non-PCM and PCM solvent models. All calculations were computed at the wB97XD/6−311++G** theory level. (A) and (B) represent the IRC and RMS, respectively, in a non-solvated system. (C) and (D) represent the IRC and RMS, respectively, in a solvated system with the PCM solvent model. In all cases, the reactions occur following the SN_2-I mechanism.

defined to study the reaction mechanisms of TEP: (i) a system consisting of a TEP molecule with some water molecules, and (ii) another system with a TEP molecule with some water molecules, using the PCM solvent model (mixed solvation approach). Using these approaches, we avoid the proton transfer problems observed in the gas phase, and it also allows us to study the effect of PCM solvent on reaction mechanisms. The results obtained for the behavior of the first hydrolysis reaction (FHR) that occurs with both the SN$_2$−I mechanism (Fig. 5) and SN$_2$−R mechanism (Fig. 6) will be discussed in detail, while for the other hydrolysis steps it can be extrapolated due to exhibiting similar behaviors (see Figure SM11).

The results show the presence of HIs for the TEP hydrolysis reaction regardless of the model approached to explore the SN$_2$−I mechanism. The formation of these hidden intermediates only occurs when the proton is present between the oxygens under the following conditions: (i) H$_2$O−H$_2$O (HO−H−OH), (ii) TEP-H$_2$O (O=PO−H−OH), (iii) ethanol-H$_2$O (−CO−−H−OH), and (iv) protonated ethanol. In addition, those endothermic reactions observed in the gas phase present in all stages of hydrolysis (THR, SHR and

FHR) were avoided, since the presence of explicit water molecules promotes a proton-transfer mechanism leading to exothermic reactions. By using the PCM solvent model, it is observed that this HI increases its stability suggesting that PCM solvent stabilizes hidden intermediates (see Fig. 5b and d).

When analyzing the reactions that occur via the SN$_2$-R mechanism, we observed the absence of HIs (Fig. 6b) even when the PCM solvent model is used (Fig. 6d). Therefore, the results obtained allow us to infer that the absence of HI is a key feature to characterize the hydrolysis reaction that occurs through the SN$_2$−R mechanism. In other words, the SN$_2$−I mechanism tends to form HI, while the SN$_2$−R mechanism avoids them.

In summary, the results of each step of the reaction in aqueous solution (THR, SHR and FHR) for the different TEP conformers for a reaction with the SN$_2$−I mechanism, show a tendency to form protonated alcohol as a reaction product, which subsequently is stabilized by the proton-transfer mechanism. On the other hand, the presence of reaction hidden intermediates decreases considerably for reaction with the SN$_2$−R mechanism and, in the product,
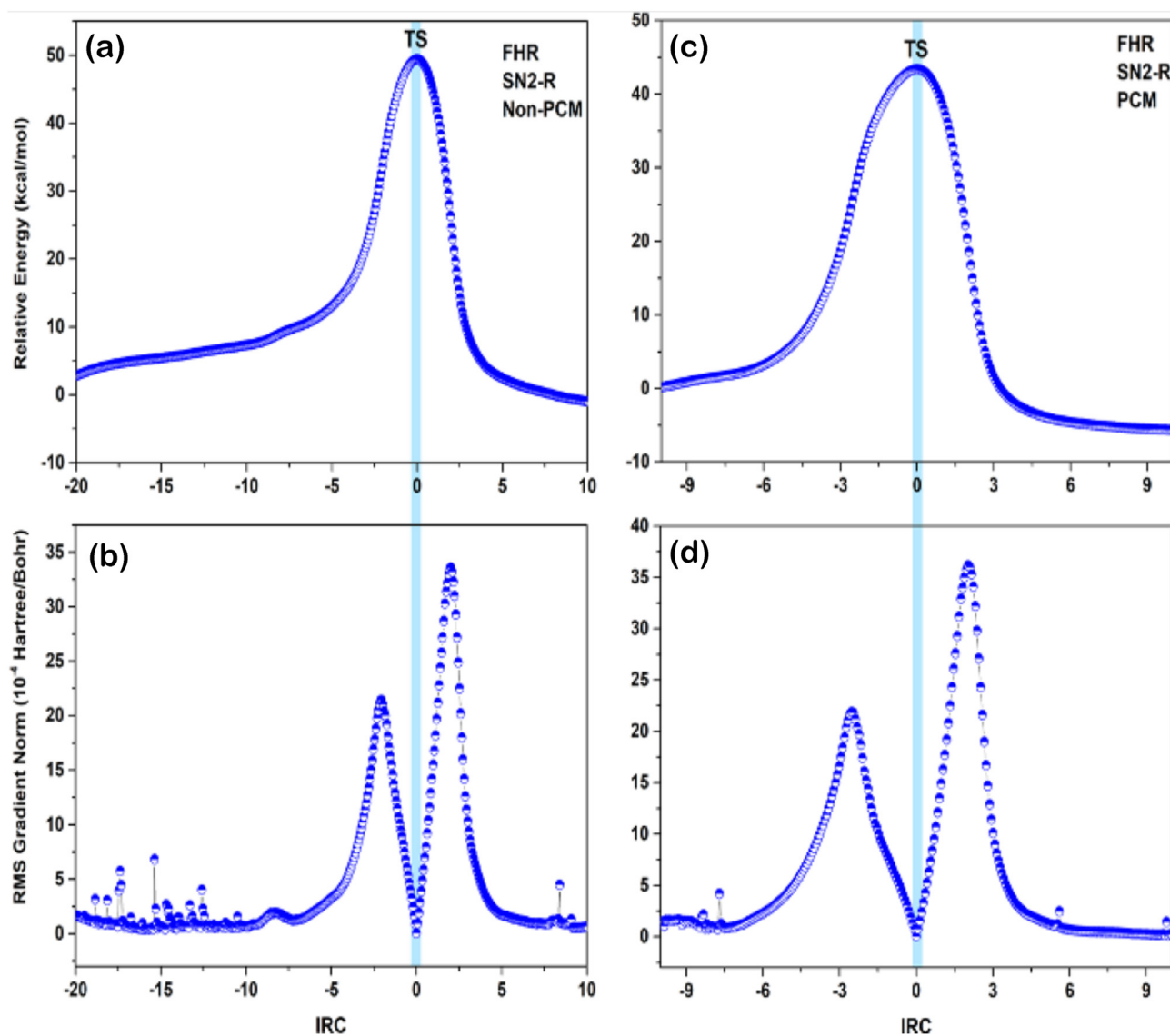
Fig. 6. IRC path energy profile and RMS gradient norm along with IRC. It is shown the reaction pathway for the reaction of hydrolysis of the TEP (FHR) with non-PCM and PCM models solvent. All calculations were computed at the wB97XD/6−311++G** theory level. (a) and (b) represent the IRC and RMS, respectively, in a non-solvated system. (c) and (d) represent the IRC and RMS, respectively, in a solvated system with the PCM solvent model. In all cases the reactions occur following the SN2-R mechanism.

O.M. Vargas Machuca Bueno, M.A. San-Miguel, C.A. Bertran et al.

Materials Today Chemistry 24 (2022) 100929

alcohol is formed directly without the exchange of protons with the solvent. Considering our findings, it was possible to describe in detail the hydrolysis reaction mechanisms for TEP molecules through the SN_2-I and SN_2-R mechanisms. By way of demonstration, we will discuss the case of the second hydrolysis reaction of TEP (Fig. 7).

In the nucleophilic attack, it is observed that the formation and breakage of chemical bonds (Fig. 7a and d) occurs more

synchronously in SN_2-I than in the SN_2-R mechanism. In addition, the TS structure forms a trigonal plane only when the reaction occurs with the SN_2-I mechanism (Fig. 7, with the atoms H, H, C, and C). Later, in the SN_2-I mechanism, it is observed that the inversion occurs symmetrically along the IRC path, inverting from $+50°$ to $-50°$ (Fig. 7e). It is worth mentioning that similar behaviors for the SN_2-I mechanism with little steric hindrance were observed by Kowalewski et al. [49].
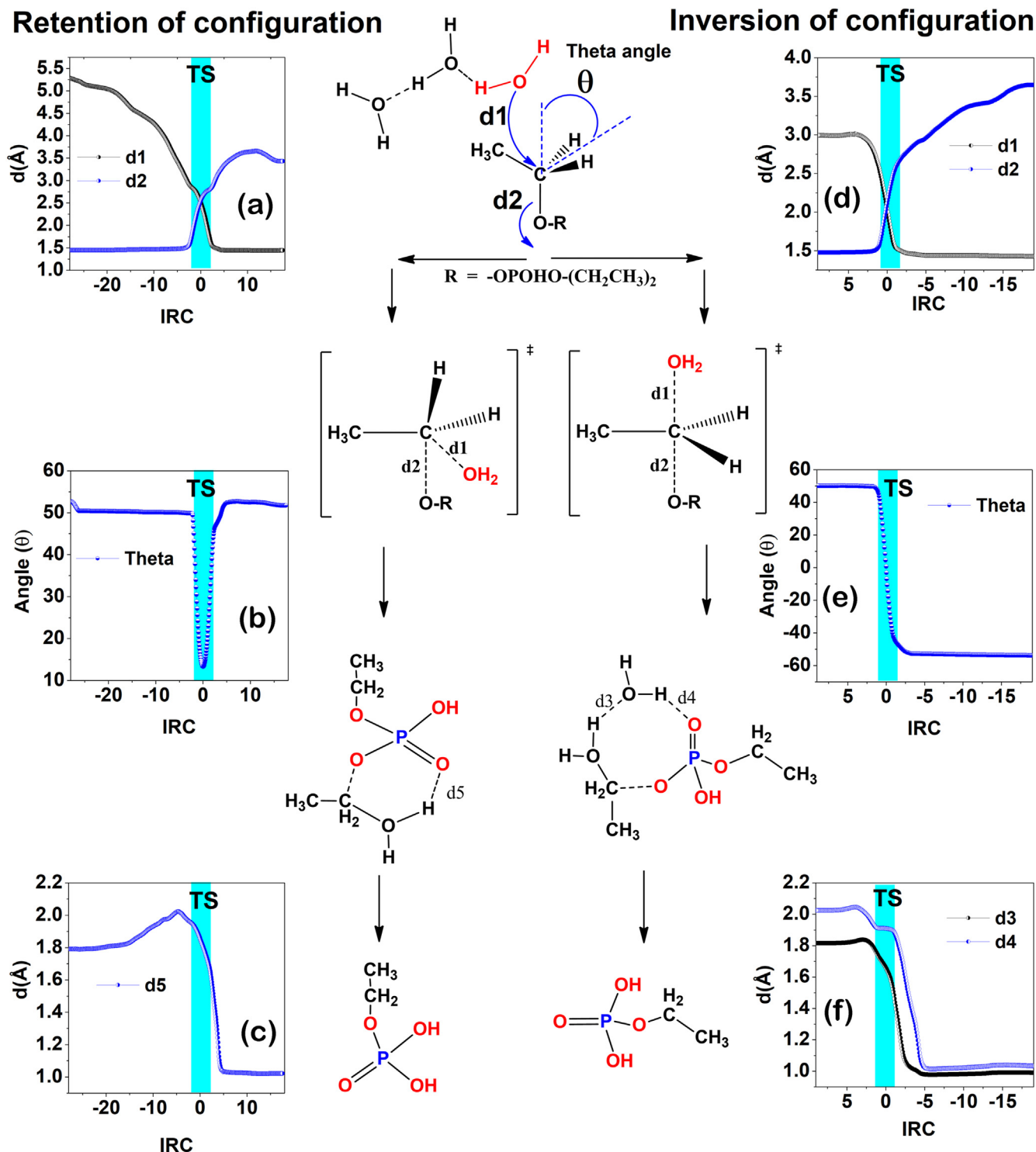

Fig. 7. Reaction mechanisms for the second hydrolysis reaction of the TEP, left (SN_2-R), and right (SN_2-I).

O.M. Vargas Machuca Bueno, M.A. San-Miguel, C.A. Bertran et al.

Materials Today Chemistry 24 (2022) 100929

Table 1
The reaction rates for each stage of TEP hydrolysis ($\Delta G^{\ddagger}_{FHR}$, $\Delta G^{\ddagger}_{SHR}$ and $\Delta G^{\ddagger}_{THR}$) obtained at 25 °C for the different categories of models studied associated with the SN$_2$−I and SN$_2$−R mechanisms.

Systems		Energy of activation (kcal·mol^{-1})					
		SN$_2$−I			SN$_2$-R		
Category	Type	$\Delta G^{\ddagger}_{FHR}$	$\Delta G^{\ddagger}_{SHR}$	$\Delta G^{\ddagger}_{THR}$	$\Delta G^{\ddagger}_{FHR}$	$\Delta G^{\ddagger}_{SHR}$	$\Delta G^{\ddagger}_{THR}$
C1	**S1**: 1TEP+1H$_2$O	53.33	52.48	51.77	60.64	59.93	58.67
	S2: 1TEP+1H$_2$O+1H$^+$	23.28	21.81	18.97	39.94	48.16	44.51
C2	**S3**: 1TEP+1H$_2$O + PCM	35.89	35.69	34.92	54.51	52.58	50.56
	S4: 1TEP+1H$_2$O+1H$^+$+PCM	21.11	20.68	19.38	35.51	35.54	40.16
C3	**S5**: 1TEP+8H$_2$O	−	−	−	49.41	55.52	49.13
	S6: 1TEP+8H$_2$O+H$^+$	−	−	−	40.33	41.70	37.96
C4	**S7**: 1TEP+8H$_2$O + PCM	28.45	28.93	29.21	43.36	45.07	48.66
	S8: 1TEP+8H$_2$O+H$^+$+PCM	20.48	20.52	20.91	34.21	33.60	37.87

While for the SN$_2$-R mechanism, it is observed that the partial configuration inversion occurs asymmetrically along the IRC path (Fig. 7b, and for other cases see Figure SM12). Furthermore, the partial configuration inversion occurs up to a maximum of ~12° (+50° → +12°), which corresponds to 38% of the investment before returning to its initial configuration.

Ultimately, when the water enters the −CH$_2$− groups as a nucleophile in the SN$_2$−I mechanism, it loses one of its protons due to the proton-transfer mechanism through the solvent (Fig. 7f, d3), and synchronously the solvent gives proton to the O=P- group (Fig. 7f, d4). Other cases are depicted in the supplementary material (see Figure SM13). In the case of the SN$_2$-R mechanism, the water entering the −CH$_2$− group as a nucleophile loses one of its protons directly by transferring it to the O=P- group, without requiring the proton-transfer mechanism through the solvent (Fig. 7c, d5).

3.2.3. Kinetic studies

For the kinetic study, we propose four categories of systems (including mixed and continuum solvent models) to study the kinetics of TEP hydrolysis and hence avoid interpretations that are biased by the type of system chosen, as discussed by Ryu and collaborators [50]. In the first category (C1), the systems are in the gas phase: S1 (1TEP + 1H$_2$O) and S2 (1TEP + 1H$_2$O + 1H$^+$). In the second category (C2), the same systems of the first category are used, but now, using the PCM solvent model: S3 (1TEP + 1H$_2$O + PCM) and S4 (1TEP + 1H$_2$O + 1H$^+$ + PCM). In the third category (C3), the systems are with more water molecules: S5 (1TEP + 8H$_2$O) and S6 (1TEP + 8H$_2$O + 1H$^+$). In the fourth category (C4), the same systems of the third category were used, but now, using the PCM solvent model: S7 (1TEP + 8H$_2$O + PCM) and S8 (1TEP + 8H$_2$O + 1H$^+$ + PCM). All protonated systems were constructed leaving the proton strategically close to the O=P- group as the MD simulations suggested.

The activation energy barrier ($\Delta G^{\ddagger}$) obtained from the potential energy curve along the IRC path are summarized in Table 1, whereas the rates of reaction of all the studied systems are displayed in Table 2.

In general, a common feature for all categories (C1−C4) can be observed, characterized by very high activation energy barriers and hence a slow reaction kinetics for both SN$_2$ mechanisms. When the systems are protonated, the activation energy barriers decrease considerably, but despite this, the barriers remain high enough to allow reactions in short times. By comparing the kinetic parameters of reactions via SN$_2$−R and SN$_2$−I mechanisms, we observe that those that occur via SN$_2$−R always present much smaller reaction rates than those that occur via the SN$_2$−I mechanism. Similar behavior can be observed for both neutral and protonated systems, i.e., the reactions that occur with SN$_2$−I are always kinetically more favored. By way of demonstration, we will approach the kinetic behavior of the third hydrolysis reaction (THR) that occurs via the SN$_2$−R mechanism for all categories (Fig. 8).

For the C1 category and in the THR stages (via SN$_2$−R), an activation energy barrier around it ~60.0 kcal mol^{-1} (S1 system) is observed, whereas a decrease of approximately 14.1 kcal mol^{-1} can be noticed for its protonated system (S2) (Fig. 8a). Although there is a considerable decrease in the energy barrier, it is not large enough to make this reaction kinetically favorable. In other words, the results show that the kinetics for the hydrolysis of TEP in the gas phase occurs with slow kinetics for both the protonated and non-protonated systems. Indeed, the calculated values for the reaction rates are very small, which for practical purposes indicates that TEP hydrolysis reactions do not occur. Similar behaviors are observed for the other reaction stages (SHR and FHR). It is noteworthy that the reaction rates that occur via the SN$_2$−I mechanism are much higher than those obs

Table 2
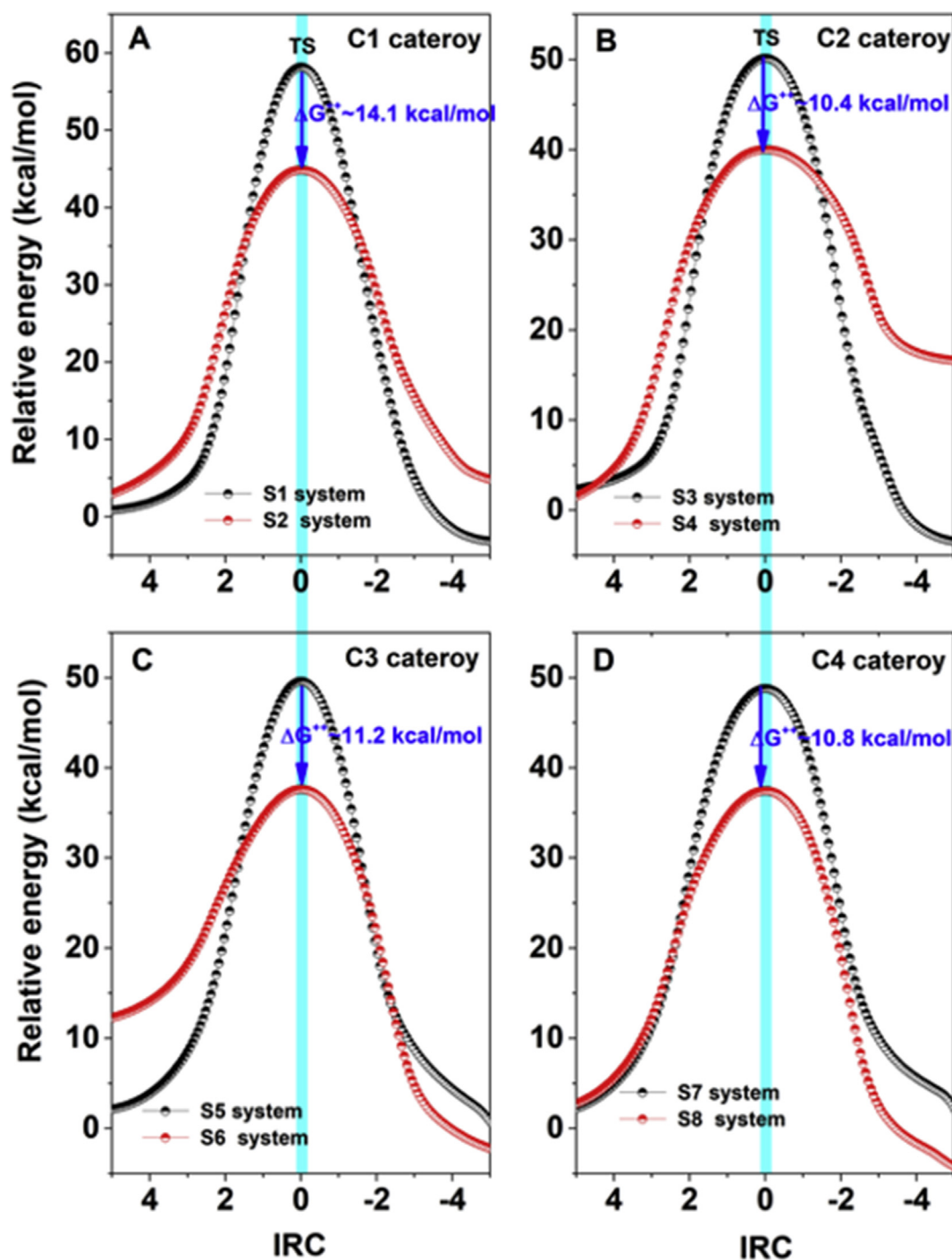The reaction rates for each stage of TEP hydrolysis (k_{FHR}, k_{SHR} and k_{THR}) were obtained at 25 °C for the different categories of models studied associated with the SN$_2$−I and SN$_2$−R mechanisms. The kinetic parameters for TEP hydrolysis reactions that occur via the SN$_2$−I mechanism were determined in our previous work [18] and included to be compared with the SN$_2$-R mechanism.

Systems		Rate of reaction (s^{-1})					
		SN$_2$−I			SN$_2$−R		
Category	Type	k_{FHR}	k_{SHR}	k_{THR}	k_{FHR}	k_{SHR}	k_{THR}
C1	**S1**: 1TEP+1H$_2$O	5.4×10^{-27}	2.3×10^{-26}	8.0×10^{-26}	2.3×10^{-32}	7.8×10^{-32}	6.56×10^{-31}
	S2: 1TEP+1H$_2$O+1H$^+$	5.8×10^{-5}	6.9×10^{-4}	8.4×10^{-2}	3.5×10^{-17}	3.3×10^{-23}	1.6×10^{-20}
C2	**S3**: 1TEP+1H$_2$O + PCM	3.6×10^{-14}	5.1×10^{-14}	1.8×10^{-13}	7.3×10^{-28}	1.9×10^{-26}	5.8×10^{-25}
	S4: 1TEP+1H$_2$O+1H$^+$+PCM	2.4×10^{-3}	4.9×10^{-3}	4.4×10^{-2}	6.2×10^{-14}	5.9×10^{-14}	2.4×10^{-17}
C3	**S5**: 1TEP+8H$_2$O	−	−	−	4.0×10^{-24}	1.3×10^{-28}	6.5×10^{-24}
	S6: 1TEP+8H$_2$O+H$^+$	−	−	−	1.8×10^{-17}	1.8×10^{-18}	9.9×10^{-16}
C4	**S7**: 1TEP+8H$_2$O + PCM	1.9×10^{-9}	4.7×10^{-9}	2.9×10^{-9}	1.2×10^{-19}	6.8×10^{-19}	1.6×10^{-20}
	S8: 1TEP+8H$_2$O+H$^+$+PCM	7.0×10^{-3}	6.8×10^{-3}	3.5×10^{-3}	6.2×10^{-13}	1.7×10^{-12}	3.3×10^{-12}

O.M. Vargas Machuca Bueno, M.A. San-Miguel, C.A. Bertran et al.

Materials Today Chemistry 24 (2022) 100929

Fig. 8. IRC path energy profile of the third TEP hydrolysis reaction occurring with the SN$_2$−R reaction mechanism. (a−d) show the IRC path energy for the four types of systems that were defined in Tables 1 and 2 (C1, C2, C3 and C4).

erved for SN$_2$-R (Table 2), which suggests that TEP hydrolysis occurs preferentially through SN$_2$−I-type mechanisms.

In the C2 category, the S3-system exhibits a barrier of ~50.0 kcal mol^{-1}, which is a high barrier to allow reactions with fast kinetics, while decreasing ~10.4 kcal mol^{-1} for the protonated system (S4) (Fig. 8b). Similar behavior is observed for the C3 category, the S5 system shows a barrier of ~49.1 kcal mol^{-1}, exhibiting a decrease of ~11.2 kcal mol^{-1} for the protonated system (S6) (Fig. 8c). Although a notable decrease in the energy barrier is observed for both categories (C2 and C3) in the protonated systems, it is still high to allow the TEP hydrolysis reaction to proceed appreciably.

The S7 system (C4 category and the mixed solvation model) exhibits a barrier of ~48.6 kcal mol^{-1}, which corresponds to a kinetic constant of 1.6×10^{-20} s^{-1} (Fig. 8d), confirming the slowness of the hydrolysis reaction via the SN$_2$−R mechanism, being even slower for the SN$_2$−I mechanism (Table 2). In the protonated system (S8), the observed kinetic constant has a value of k$_{(THR)}$ = 3.3×10^{-12} s^{-1}. Although these constants have shown a considerable reduction as the systems were protonated, their values still remain high, indicating slow kinetics. A similar result can be observed for systems that follow the SN$_2$−I mechanism. When compared with the continuum solvation model (C2 category,

S3 system), we also found discrepancies between the two models in predicting the activation energy barrier, as reported by Ho Ryu et al. [50] Here, the mixed solvation model also tends to predict smaller barriers than the continuum solvation model.

3.3. Effect of the mechanism and kinetics of TEP hydrolysis reaction on the formation of the vitreous network

The synthesis of alkaline-earth phosphosilicate bioactive glasses materials by the sol-gel process includes hydrolysis reactions of alkoxide precursors (alkoxysilane and alkoxyphosphate) and condensation of hydrolyzed species to form colloidal suspensions with calcium ions (network-modifier ion) anchored in the silicophosphate particles [14]. The reactions between the colloidal particles lead to the formation of the gel network of calcium silica phosphate with the solvent, embedding the pores and subsequent drying and calcination steps lead to the formation of the vitreous material [18,19]. The rate of gel formation depends on several parameters such as pH, temperature and molar ratio of the precursor, water and solvent [51,52].

Several studies have been addressed to study the kinetics in the acid- or base-catalyzed hydrolysis of TEOS [51–53] The kinetic constants for the hydrolysis and condensation reactions of the silicon precursor ($TEOS \overset{K_H}{\leftrightarrow} Si(OH)_4 \overset{K_C}{\leftrightarrow} SiO_2$) suggest faster kinetics for both processes compared to either of these reactions for triethyl phosphate, regardless of the experimental conditions [18,51–53] As a result, the formation of the silica particles occurs in a much shorter time scale than that necessary for the TEP hydrolysis reaction to occur, considering the reaction conditions of synthesis for 58S bioactive glass. In this scenario, as silica structures grow, non-hydrolyzed triethyl phosphate molecules are continuously expelled from the silica matrix, accumulating at the particle interfaces. The presence of domains rich in silica and phosphate species present in the xerogel structure remains segregated into domains in the vitreous matrix during the calcination stage (Figure SM14). The proximity of the phosphate species in the interstices of the silica particles (precursor of the silica backbone) combined with the low diffusion coefficient of the PO_4^{3-} group in the glass favors the formation of polymerized species of phosphates. The incorporation of network modifiers (calcium) during calcination leads to the formation of a glassy portion rich in the silicate network, while part of the Ca^{2+} forms crystalline domains composed of calcium pyrophosphate [54–56].

The presence of heterogeneity in the vitreous matrix has a profound impact on the biological behavior of bioactive glass as part of the biologically active species. They are trapped within the crystalline lattices of the matrix and cannot be leached into the medium [18,54,55,57]. The presence of insoluble aggregates in the microstructure of bioactive glasses can result in the transition from a highly bioactive to bioinactive composition since they modify the structure and composition of the glass surface and changes the energy barriers for ionic migration [58–60]. Indeed, a huge number of works in the literature address the use of bioactive glasses for ionic therapy due to their proven ability to deliver ions capable of stimulating genes of cells towards a path of regeneration and self-repair [4,61–65].

4. Conclusions

Classical molecular dynamics simulations aimed to explore the conformers of the TEP molecule, endorsing a synopsis of the interaction of the TEP molecule with the solvent, and allowing to propose different potential reaction routes, which were also confirmed from DFT calculations. It was found that the hydrolysis of TEP occurs via both SN_2-I and SN_2-R mechanisms. Our findings show that the

activation energy barrier involved in the TEP hydrolysis reaction is considerably high. Furthermore, the activation barrier for the SN_2-R mechanism is considerably higher compared to the same reaction via SN_2-I. Consequently, the highest reaction rates (k_{FHR}, k_{SHR} and k_{THR}) for all hydrolysis stages observed for the SN_2-I mechanism. Hence, SN_2-I is the kinetically favored mechanism, making it the main reaction path for the TEP reaction. Although the kinetic constants for SN_2-I are greater than those described for the SN_2-R mechanism, they remain to indicate slow kinetics for TEP hydrolysis. This behavior was found for all three TEP hydrolysis reactions, regardless of whether the system was protonated or non-protonated. This result has a profound influence on the microstructure of the xerogel that will give rise to the bioactive glass matrix during the calcination step. The unhydrolyzed triethyl phosphate molecules tend to be expelled as the gel network is formed, accumulating at the interfaces of the silica particles. The proximity of phosphate species in the interstices of silica particles favours the formation of polymerized phosphate species (bioinactive calcium pyrophosphates) during the calcination step, resulting in glasses with low microstructural homogeneity.

CRediT authorship contribution statement

Otto V. M. Bueno: conceptualization, data curation, formal analysis, investigation, validation, methodology, and original article. Miguel A. San-Miguel: formal analysis, investigation, validation, supervision, project administration, resources, and original draft. Celso A. Bertran: visualization and reviewing and editing the article. Edison Z. da Silva: supervision; visualization and reviewing and editing the article. Joao H. Lopes: conceptualization, data curation, formal analysis, investigation, validation, methodology, supervision, and original article.

Declaration of competing interest

The authors declare that they have no known competing financial interests or personal relationships that could have appeared to influence the work reported in this paper.

Acknowledgements

Appendix A. Supplementary data

Supplementary data to this article can be found online at https://doi.org/10.1016/j.mtchem.2022.100929.

References

[1] Q. Chen, et al., Tissue Engineering Scaffolds from Bioactive Glass and Composite Materials, 2008.
[2] F. Baino, et al., J. Funct. Biomater. 9 (1) (2018).
[3] M. Cong, et al., Biomed. Mater. 10 (2) (2015), 025005.
[4] L.L. Hench, J. Eur. Ceram. Soc. 29 (7) (2009) 1257.
[5] K. Zheng, A.R. Boccaccini, Adv. Colloid Interface Sci. 249 (2017) 363.

O.M. Vargas Machuca Bueno, M.A. San-Miguel, C.A. Bertran et al.

Materials Today Chemistry 24 (2022) 100929

[6] J.R. Jones, Bioactive glass as synthetic bone grafts and scaffolds for tissue engineering, in: Bio-Glasses, John Wiley & Sons, 2012, p. 177.
[7] L. Gerhardt, A.R. Boccaccini, Materials 3 (7) (2010) 3867.
[8] M.T. Dehaghani, et al., Int. J. Appl. Ceram. Technol. 12 (4) (2015) 867.
[9] L. Ji, et al., Mater. Sci. Eng. C 75 (2017) 590.
[10] J.H. Lopes, et al., Eur. Polym. J. 116 (2019) 425.
[11] F. Baino, et al., Int. J. Appl. Ceram. Technol. 15 (4) (2018) 841.
[12] N. Gupta, D. Santhiya, Mesoporous bioactive glass and its applications, in: H. Ylänen (Ed.), Bioactive Glasses, Woodhead Publishing, 2018, p. 63.
[13] A.J. Aho, et al., J. Mater. Sci. Mater. Med. 15 (10) (2004) 1165.
[14] K. Deshmukh, et al., RSC Adv. 10 (56) (2020) 33782.
[15] S. Izadi, et al., Int. J. Mater. Res. 106 (3) (2014) 301.
[16] A. Tilocca, A.N. Cormack, J. Phys. Chem. B 111 (51) (2007) 14256.
[17] W.-C. Chen, et al., Materials (Basel, Switzerland) 6 (11) (2013) 5335.
[18] O.M.V.M. Bueno, et al., Mater. Sci. Eng. C 120 (2021) 111759.
[19] J.H. Lopes, et al., Mater Sci Eng C Mater Biol Appl 97 (2019) 669.
[20] S. Neupane, et al., J. Phys. Chem. A 123 (22) (2019) 4764.
[21] A. Tilocca, J. Mater. Chem. 20 (33) (2010) 6848.
[22] S. Neupane, et al., J. Phys. Chem. A 122 (15) (2018) 3829.
[23] C. Ruan, et al., J. Phys. Chem. A 111 (51) (2007) 13521.
[24] B.S. Fales, et al., J. Am. Soc. Mass Spectrom. 22 (10) (2011) 1862.
[25] M.J. Frisch, et al., Gaussian 09 Rev, . D.01, Wallingford, CT, 2009.
[26] K. Fukui, J. Phys. Chem. A 74 (23) (1970) 4161.
[27] K. Fukui, Accounts Chem. Res. 14 (12) (1981) 363.
[28] S. Maeda, et al., Int. J. Quant. Chem. 115 (5) (2015) 258.
[29] R. Xiao, et al., Int. J. Quant. Chem. 114 (1) (2014) 74.
[30] R.P. Bell, Trans. Faraday Soc. 55 (1959) 1.
[31] I.T. Todorov, et al., J. Mater. Chem. 16 (20) (2006) 1911.
[32] H.A. Posch, et al., Phys Rev A 33 (6) (1986) 4253.
[33] L. Martínez, et al., J. Comput. Chem. 30 (13) (2009) 2157.
[34] L.S. Dodda, et al., Nucleic Acids Res. 45 (W1) (2017) W331.
[35] G.A. Kaminski, et al., J. Phys. Chem. B 105 (28) (2001) 6474.
[36] L.S. Dodda, et al., J. Phys. Chem. B 121 (15) (2017) 3864.
[37] W.L. Jorgensen, J. Am. Chem. Soc. (1981) 335. Medium: X; Size.
[38] W.D. Cornell, et al., J. Am. Chem. Soc. 117 (19) (1995) 5179.
[39] S. Urata, et al., J. Phys. Chem. B 109 (9) (2005) 4269.
[40] S. Cui, et al., J. Phys. Chem. B 111 (9) (2007) 2208.
[41] S.V. Sambasivarao, O. Acevedo, J. Chem. Theor. Comput. 5 (4) (2009) 1038.
[42] C. Cadena, E.J. Maginn, J. Phys. Chem. B 110 (36) (2006) 18026.
[43] A.P. Thompson, et al., Comput. Phys. Commun. 271 (2022) 108171.
[44] G.A. Tribello, et al., Comput. Phys. Commun. 185 (2) (2014) 604.
[45] J.F. Dama, et al., Phys. Rev. Lett. 112 (24) (2014) 240602.
[46] A.J. Ilott, et al., J. Phys. Chem. B 117 (40) (2013) 12286.
[47] G.A. Tribello, et al., J. Chem. Theor. Comput. 13 (3) (2017) 1317.
[48] M. Brehm, B. Kirchner, J. Chem. Inf. Model. 51 (8) (2011) 2007.
[49] M. Kowalewski, et al., J. Phys. Chem. A 118 (26) (2014) 4661.
[50] H. Ryu, et al., Organometallics 37 (19) (2018) 3228.
[51] J.C. Echeverría, et al., J. Sol. Gel Sci. Technol. 86 (2) (2018) 316.
[52] G. De, et al., J. Mater. Chem. 10 (10) (2000) 2289.
[53] S.-L. Chen, et al., Ind. Eng. Chem. Res. 35 (12) (1996) 4487.
[54] J.H. Lopes, et al., Ceram. Int. 48 (6) (2022) 8039.
[55] J.H. Lopes, et al., Mater Sci Eng C Mater Biol Appl 72 (2017) 86.
[56] J.H. Lopes, et al., J. Am. Ceram. Soc. 96 (5) (2013) 1464.
[57] A. Tilocca, Phys. Rev. B 76 (22) (2007).
[58] A. Tilocca, J. Chem. Phys. 133 (1) (2010), 014701.
[59] A. Tilocca, et al., Faraday Discuss 136 (2007) 45.
[60] A. Tilocca, et al., Chem. Mater. 19 (1) (2007) 95.
[61] F.V. Ferreira, et al., Mater Sci Eng C Mater Biol Appl 123 (2021) 111853.
[62] J.H. Lopes, et al., J. Biomed. Mater. Res. B Appl. Biomater. 108 (4) (2020) 1372.
[63] L.P.L. de Souza, et al., J. Biomed. Mater. Res. 108 (3) (2020) 446.
[64] F.V. Ferreira, et al., Nanoscale 11 (42) (2019) 19842.
[65] L. Souza, et al., Sci. Rep. 8 (1) (2018) 12808.